JUSTC

Article

http://justc.ustc.edu.cn

Received: April 24, 2024; Accepted: August 09, 2024

Modeling and analysis of a novel oxygen production approach with full-spectrum solar energy for the lunar human base

Wei Zhu, and Maobin Hu ✉

School of Engineering Science, University of Science and Technology of China, Hefei 230026, China

✉Correspondence: Maobin Hu, E-mail: humaobin@ustc.edu.cn

Graphical abstract

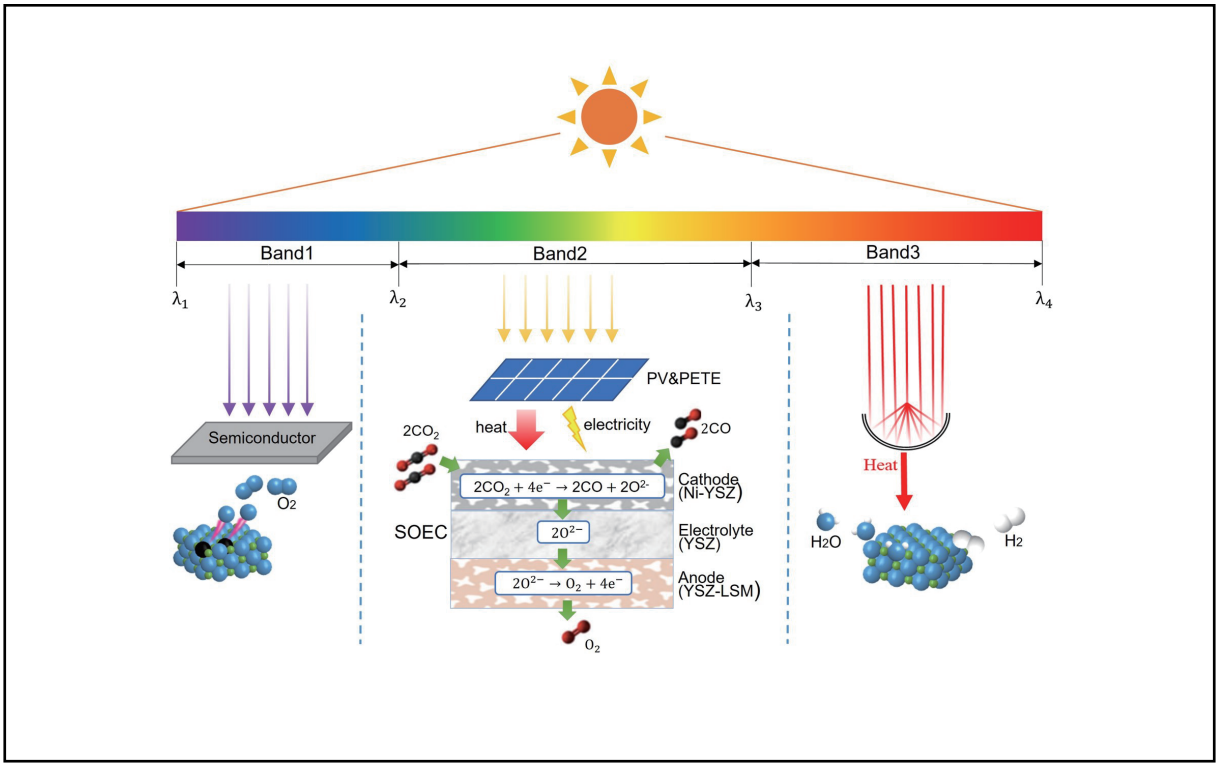

Schematic diagram of solar full-spectrum split-frequency oxygen generation system.

Public summary

- Combining PV and PETE for the first time to utilize carbon dioxide electrolysis to produce oxygen at high temperature. By using medium–low temperature PV and high temperature PETE to heat carbon dioxide and convert part of the solar energy into electricity, respectively, high temperature carbon dioxide electrolysis for oxygen production is realized.

- Utilizing solar energy on the Moon to achieve in-situ resource utilization and to make full use of the full spectrum of solar energy, i.e., UV and IR bands for photo- and thermo-reactions, respectively, and visible band for photovoltaic/PETE modules.

- The full utilization of carbon dioxide and water vapor produced by human respiration to obtain oxygen through two pathways: electrolysis of carbon dioxide in SOEC and decomposition of water vapor through photothermal synergistic reaction.

Citation: Zhu W, Hu M B. Modeling and analysis of a novel oxygen production approach with full-spectrum solar energy for the lunar human base. *JUSTC*, **2025**, 55(2): 0201. CSTR: 32290.14.JUSTC-2024-0062. DOI: 10.52396/JUSTC-2024-0062

JUSTC

Article

http://justc.ustc.edu.cn

Received: April 24, 2024; Accepted: August 09, 2024

Modeling and analysis of a novel oxygen production approach with full-spectrum solar energy for the lunar human base

Wei Zhu, and Maobin Hu ✉

School of Engineering Science, University of Science and Technology of China, Hefei 230026, China

✉Correspondence: Maobin Hu, E-mail: humaobin@ustc.edu.cn

Cite This: *JUSTC*, **2025**, 55(2): 0201 (16pp)

Read Online

Abstract: Building a lunar human base is one of the important goals of human lunar exploration. This paper proposes a method for the production of oxygen by combining photothermal synergistic water decomposition with high-temperature carbon dioxide electrolysis, utilizing the full solar spectrum. The optimal oxygen production rates under different solid oxide electrolysis cell inlet temperatures T_e, ultraviolet (UV) separation wavelengths λ_2, infrared (IR) separation wavelengths λ_3, and photovoltaic cell materials were explored. The results indicate that the inlet temperature of the solid oxide electrolysis cell should be as high as possible so that more carbon dioxide can be converted into carbon monoxide and oxygen. Furthermore, when the ultraviolet separation wavelength is approximately 385 nm, the proportion of solar energy allocated to the photoreaction and electrolysis cell is optimal, and the oxygen production rate is highest at 2.754×10^{-4} mol/s. Moreover, the infrared separation wavelength should be increased as much as possible within the allowable range to increase the amount of solar radiation allocated to the electrolysis cell to improve the rate of oxygen generation. In addition, copper indium gallium selenide (CIGS) has a relatively large separation wavelength, which can result in a high oxygen production rate of 3.560×10^{-4} mol/s. The proposed integrated oxygen production method can provide a feasible solution for supplying oxygen to a lunar human base.

Keywords: lunar oxygen production; full-spectrum solar energy; photovoltaic and photon-enhanced thermionic emission; electrolysis of carbon dioxide; photothermal synergistic reaction; solid oxide electrolysis cell

CLC number: TK519 **Document code:** A

1 Introduction

The exploration of the Moon and the establishment of a lunar human base on the Moon have always been important goals in the field of space exploration. Since the successful landing of Apollo 11 on the Moon in 1969, many lunar exploration missions have been carried out, gradually revealing the mysteries of the Moon[1,2]. However, human activities on the Moon have thus far been limited to short-term exploration missions, whereas the establishment of a human base on the Moon requires more complex and long-term technological and resource support[3,4]. Among these resources, oxygen is one of the most important, as it is not only essential for human survival but also an important oxidizer and fuel in space missions[5]. Therefore, how to sustainably and efficiently utilize in situ resources on the Moon to produce oxygen has become the focus of researchers' attention. The current methods for producing lunar oxygen include chemical reduction[6,7] (using hydrogen, carbon, fluorine, methane, etc.), gas-phase pyrolysis[8], and molten oxide electrolysis[9,10]. Zhong et al.[11] demonstrated the feasibility of in situ utilization of lunar soil by efficiently providing extraterrestrial fuel and oxygen through electrocatalytic carbon dioxide conversion, with a methane yield of 0.8 mL/min and an oxygen yield of 2.3 mL/min under experimental conditions. Liu et al.[12] utilized a nickel–iron alloy anode to electrolyze a simulated lunar soil in a cryolite melt at a temperature of 1233 K to generate aluminum–silicon alloys and oxygen, and approximately 0.0021 mol of oxygen was collected in 83 s.

The Moon not only possesses utilizable in situ resources such as lunar soil and water ice but also receives much more intense solar radiation than the Earth's surface because of the absence of an atmosphere on the lunar surface and the long hours of sunshine in the equatorial region[13,14]. Therefore, the abundant solar energy resources also have considerable potential for utilization. Li et al.[15] proposed a method to efficiently utilize the full spectrum of solar energy, which combines a photovoltaic power electrolysis water reaction with a synergistic photothermal reaction to convert a large portion of the energy in the solar spectrum into high-grade electrical energy instead of thermal energy, thereby increasing the utilization of the full spectrum of solar energy. Photothermal synergistic reactions refer to the combination of photochemical reactions and thermochemical reactions, which can effectively improve the utilization rate of solar energy. The ultraviolet band of the solar spectrum is used for light reactions to irradiate the surface of semiconductor metal oxides and generate oxygen vacancies to further generate oxygen. The infrared band is used for thermal reactions. The semiconductor metal oxides generated are collected by the solar collector and

CSTR: 32290.14.JUSTC-2024-0062
DOI: 10.52396/JUSTC-2024-0062
JUSTC, **2025**, 55(2): 0201

heated in the atmosphere of water vapor so that water is decomposed and hydrogen is generated[16].

In February 2021, the U.S. Mars rover "Perseverance" successfully landed on Mars[17]. The MOXIE oxygen production system uses a solid oxide electrolysis cell to produce oxygen by electrolyzing carbon dioxide at high temperatures[18,19]. Under the ambient conditions of extraterrestrial space, an oxygen production rate of 5.37 $g \cdot h^{-1}$ was achieved[20], confirming the practical feasibility of applying the high-temperature electrolysis of carbon dioxide for oxygen production for deep space exploration[21]. For humans on the Moon, human exhaled gases can be collected, and the carbon dioxide therein can be utilized for high-temperature electrolysis to produce oxygen, realizing the carbon–oxygen cycle. However, the high-temperature source of electrolyzing carbon dioxide in the MOXIE system is nuclear power batteries, which are not suitable for use inside or near the lunar base because of their radioactivity[22]. Wang et al.[23] proposed a hydrogen production system from electrolyzed water that combines photovoltaic (PV) cells, photon-enhanced pyroelectric cells (PETEs) and solid oxide electrolysis cells (SOECs). With the waste heat recovered from the PV cells and PETE modules, the inlet steam temperature of the SOEC can be increased to 800–1000 °C, and the electricity generated can be used for high-temperature electrolysis. Similarly, the use of solar concentrators on the Moon can also realize the electrolysis of carbon dioxide to produce oxygen and carbon monoxide at high temperatures.

On the basis of the above ideas, this paper proposes a full-solar-spectrum lunar oxygen production system that combines PV/PETE power generation electrolysis of carbon dioxide and a synergistic photothermal reaction. This work creatively combines the electrolysis of carbon dioxide by SOECs with a synergistic photothermal reaction and only needs renewable solar energy to supply power for the system to produce oxygen from the carbon dioxide and water vapor generated by human respiration in the lunar human base. Moreover, the generated carbon monoxide and hydrogen can be used as fuels for production, construction, and other activities. The combination of PV cells and PETE modules produces heat and electricity while meeting the temperature requirements of carbon dioxide electrolysis. In this work, a mathematical model of this system is developed to analyze the effects of different separation wavelengths in the solar spectrum on the oxygen production rate, and the optimal conditions for obtaining the highest oxygen production rates are explored.

Compared with the literature, the contributions of this paper mainly include the following: (ⅰ) PV and PETE were combined for the first time to utilize carbon dioxide electrolysis to produce oxygen at high temperatures. By using medium–low-temperature PVs and high-temperature PETEs to heat carbon dioxide and convert part of the solar energy into electricity, high-temperature carbon dioxide electrolysis for oxygen production is realized. (ⅱ) Solar energy on the Moon is utilized to achieve in situ resource utilization and to make full use of the full spectrum of solar energy, i.e., ultraviolet (UV) and infrared (IR) bands for photo- and thermoreactions, respectively, and the visible band for photovoltaic/PETE modules. (ⅲ) Carbon dioxide and water vapor produced by human respiration are fully utilized through two pathways: electrolysis of carbon dioxide in the SOEC and decomposition of water vapor through synergistic photothermal reactions.

2 Mathematical model

The solar full-spectrum oxygen production system described in this article can be divided into two parts on the basis of the pathway of oxygen production, namely, a synergistic photothermal reaction for oxygen production and PV/PETE heating and electric power generation for electrolysis of the carbon dioxide reaction for oxygen production. The synergistic photothermal reaction can be divided into a photoreaction stage and a thermal reaction stage, whereas the PV/PETE heating and electric power generation electrolysis of carbon dioxide include the PV/PETE heating and electric power generation stage and the solid oxide electrolytic cell electrolysis of carbon dioxide stage.

2.1 Introduction of the proposed system

Fig. 1 shows the AM0 standard solar spectrum and comprehensive oxygen production method using the full solar spectrum. AM0 refers to the reception of sunlight in outer space. When sunlight reaches the upper boundary of the Earth's atmosphere, the radiant intensity decays to approximately 1367 $W \cdot m^{-2}$, which is the solar constant. The annual variation range of solar irradiance on the lunar surface is 1321.5−1416.6 $W \cdot m^{-2}$, with an average of 1367 $W \cdot m^{-2}$[24]. Therefore, it is more accurate to use the AM0 data as the solar radiation on the Moon. In the comprehensive oxygen production method, a solar spectral separator is used to divide the solar spectrum into three bands, namely, band 1, band 2, and band 3, according to the separation wavelengths λ_2 and λ_3.

Band 1 is a high-frequency photonic band used to irradiate semiconductor metal oxides M_xO_y as photocatalytic materials. Oxygen vacancies are generated on its surface, and oxygen is generated, which is the process of a photocatalytic reaction. The reaction was carried out at room temperature as follows:

$$M_xO_y \xrightarrow{\text{light}} M_xO_{y-1} + \frac{1}{2}O_2(g). \tag{1}$$

Then, band 3 in the infrared band is absorbed by the solar collector and converted into heat energy, and the M_xO_{y-1} is mixed with water and heated to 500–600 °C. The oxygen vacancies on the surface of semiconductor metal oxides react with water molecules to regenerate M_xO_y and hydrogen, i.e., the thermochemical water cracking reaction, as follows:

$$M_xO_{y-1} + H_2O(g) \xrightarrow{500-600\,^{\circ}C} M_xO_y + H_2(g). \tag{2}$$

The synergistic photothermal reaction represented by Eqs. (1) and (2) can describe the specific reaction steps by using electron molecules as the basic particles as follows[25]:

Light reaction:

$$M_xO_y + 2h\nu \rightarrow 2h^+ + 2e^-, \tag{3}$$

$$M^{\frac{2y}{x}+} + 2e^- \rightarrow M^{\frac{2(y-x)}{x}+} + V_o, \tag{4}$$

CSTR: 32290.14.JUSTC-2024-0062
DOI: 10.52396/JUSTC-2024-0062
JUSTC, **2025**, 55(2): 0201

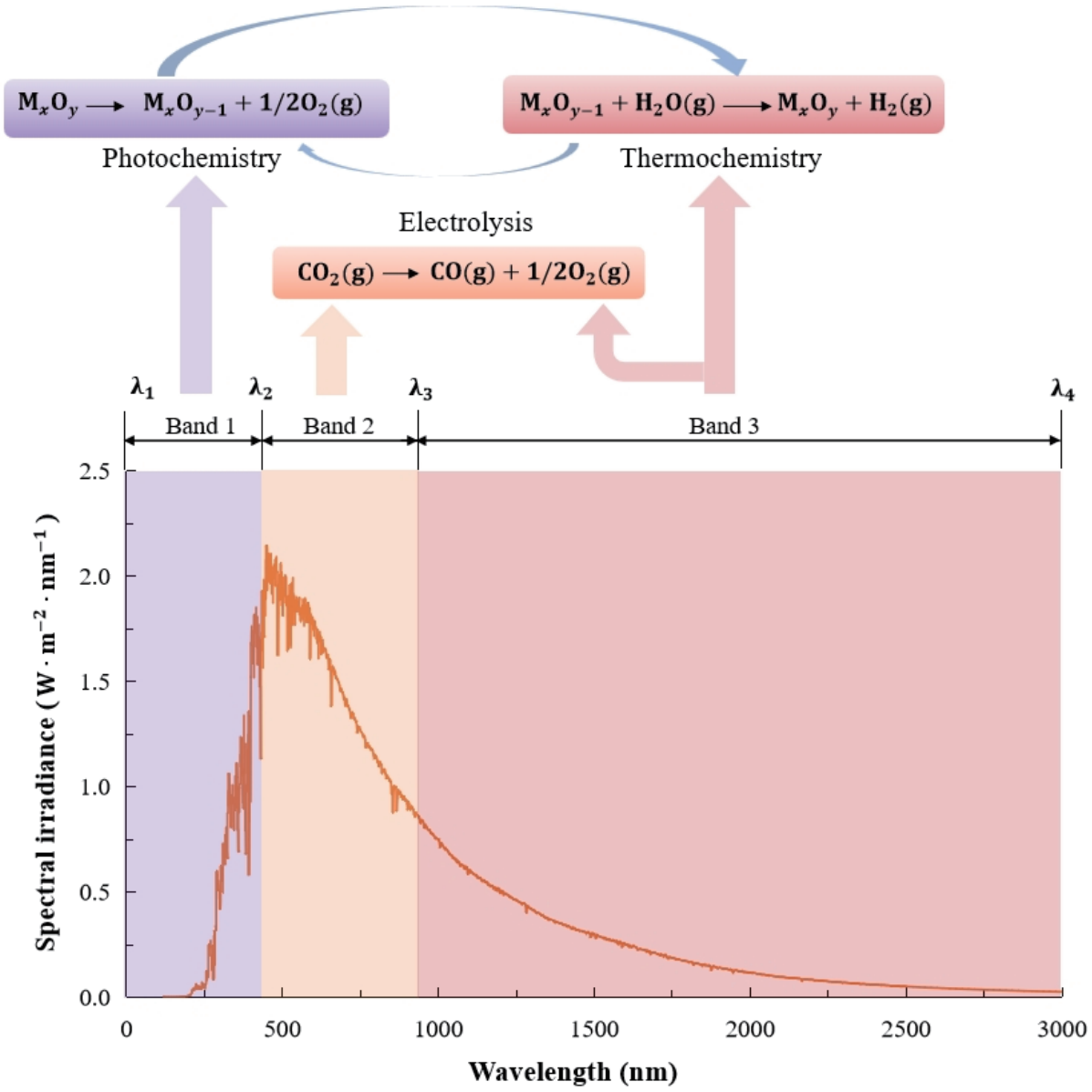

Fig. 1. Schematic of the AM0 standard solar full-spectrum comprehensive oxygen production approach.

$$O^{2-} + 2h^+ \rightarrow \frac{1}{2}O_2(ad), \tag{5}$$

$$\frac{1}{2}O_2(ad) \rightarrow \frac{1}{2}O_2(g). \tag{6}$$

Thermal reaction:

$$H_2O(g) \rightarrow H_2O(ad), \tag{7}$$

$$H_2O(ad) + \frac{1}{x}M_xO_{y-1} \rightarrow H_2(ad) + \frac{1}{x}M_xO_y, \tag{8}$$

$$H_2(ad) \rightarrow H_2(g), \tag{9}$$

where $h\nu$ stands for illumination; h^+ refers to holes; V_o represents oxygen vacancies; and (ad) represents the adsorption state. Eqs. (3)−(6) show the generation and separation process of photogenerated electron–hole pairs, the generation of oxygen vacancies and oxygen, and the process of oxygen desorption. Eqs. (7)−(9) represent the thermal reaction part, which shows that the adsorbed water molecules react with oxygen vacancies to generate hydrogen and desorb from the surface of semiconductor metal oxides.

At the same time, as a photocatalytic reaction and thermochemical reaction, heated carbon dioxide is electrolyzed in a solid oxide electrolytic cell (SOEC). Fig. 2 shows the PV/PETE−SOEC electrolytic carbon dioxide oxygen production system. The PV cells and the PETE module absorb solar energy to generate electricity, and the excess heat is recycled to heat the carbon dioxide passing through the pipeline below, increasing its temperature to the electrolysis temperature. The heated carbon dioxide is subsequently transported together with the generated electrical energy to the SOEC, where the high-temperature carbon dioxide is electrolyzed to produce

CSTR: 32290.14.JUSTC-2024-0062
DOI: 10.52396/JUSTC-2024-0062
JUSTC, **2025**, 55(2): 0201

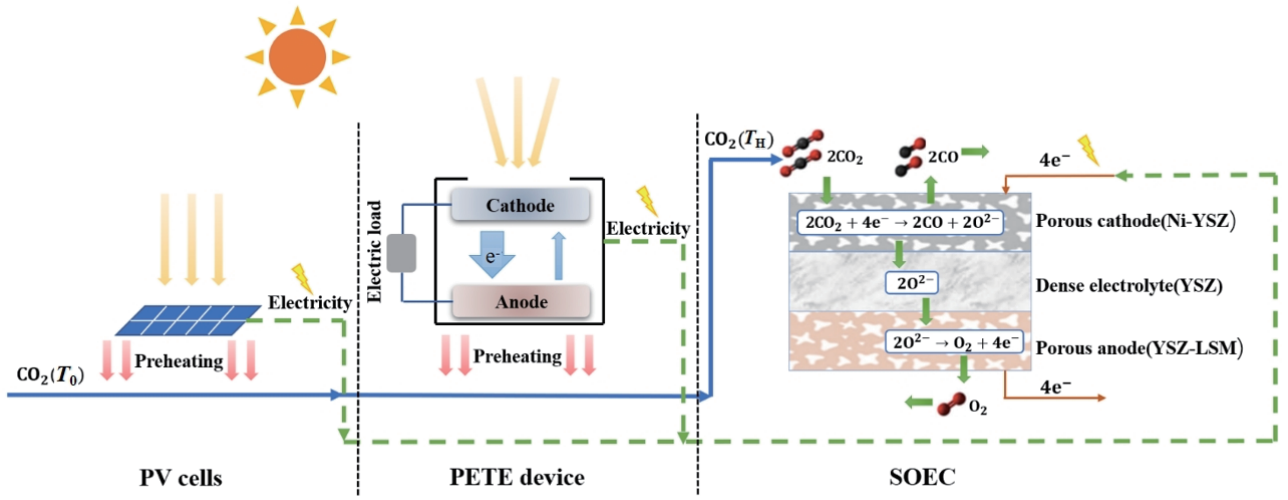

Fig. 2. PV/PETE−SOEC electrolytic carbon dioxide oxygen production system.

oxygen and carbon monoxide, and the gas is collected. The general equation for electrolytic carbon dioxide is as follows:

$$CO_2(g) \rightarrow CO(g) + \frac{1}{2}O_2(g). \tag{10}$$

Assuming that electrolysis is in an ideal state, the electrode reaction equations are shown below:

$$CO_2(g) + 2e^- \rightarrow CO(g) + O^{2-}(\text{Cathode}), \tag{11}$$

$$O^{2-} \rightarrow 2e^- + \frac{1}{2}O_2(g)(\text{Anode}). \tag{12}$$

The main assumptions in the modeling are as follows:

(Ⅰ) All the gas species are ideal gases.

(Ⅱ) The SOEC is operated in the steady state.

(Ⅲ) The gas flow in the SOEC is laminar.

(Ⅳ) Electrochemical reactions take place in the anode and cathode catalyst layers.

(Ⅴ) The effect of gravity is neglected.

2.2 Model of the photothermal synergistic reaction section

According to the principle of wave particle duality, sunlight is composed of countless photons, and the energy possessed by a photon of a specific wavelength can be expressed as follows:

$$E_p(\lambda) = h\frac{c}{\lambda}, \tag{13}$$

where h, c, and λ are the Planck constant, speed of light, and wavelength, respectively.

According to energy band theory, only when the incident photon energy $E_p(\lambda)$ is greater than the semiconductor bandgap E_g can electrons be excited from the valence band to the conduction band. Therefore, the band gap width of a material determines the cutoff absorption wavelength of the semiconductor metal oxide $\lambda_{c,abs}$, which also affects the cutoff absorption wavelength of the PV panels $\lambda_{pv,abs}$. At the same time, in the photothermal synergistic reaction, oxygen vacancies (V_o), as the link between the light reaction and the thermal reaction, introduce oxygen vacancy energy to form an energy level El_{V_o}, and there is a cutoff wavelength λ_{c,V_o}. By comparing the cutoff absorption wavelengths of semiconductor or metal oxides $\lambda_{c,abs}$ with the cutoff wavelength of oxygen vacancy formation λ_{c,V_o}, the UV separation wavelength λ_2 can be determined. Yang et al.[26] showed via density functional theory (DFT) that the oxygen vacancy formation energy level (El_{V_o}) is between the top of the valence band (VB) and the bottom of the conduction band (CB). Therefore, the cutoff wavelength of oxygen vacancy formation λ_{c,V_o} is greater than the absorption cutoff wavelength of semiconductor metal oxides $\lambda_{c,abs}$, which means that all photons with wavelengths less than $\lambda_{c,abs}$ have the ability to participate in the synergistic photothermal reaction. Therefore, the UV separation wavelength λ_2 can be used as the cutoff absorption wavelength $\lambda_{c,abs}$ of the semiconductor metal oxide, and the IR separation wavelength λ_3 can be used as the cutoff absorption wavelength $\lambda_{pv,abs}$ of the PV panel.

Next, the oxygen production rate of the synergistic photothermal reaction was analyzed. According to the solar power per unit area at a specific wavelength and the energy of a single photon $E_p(\lambda)$, the photon flux density ($PFD(\lambda)$) at a specific wavelength in the solar spectrum can be obtained, as shown in Fig. 3a. Therefore, the number of photons incident in the light reaction can be expressed as:

$$N_P = S_{lr}t_{lr}\int_{\lambda_1}^{\lambda_2} PFD(\lambda)\,d\lambda, \tag{14}$$

where S_{lr} and t_{lr} are the area of solar radiation absorbed in the light reaction and the time taken for the light reaction to absorb radiation, respectively.

However, the incident photons are not all absorbed. The ability of semiconductor metal oxides to absorb photons depends on the absorption coefficient $r_{abs}(\lambda)$, which can be obtained via UV–visible diffuse reflection absorption spectrometry. Montoya et al.[27] obtained reflection spectrum data of a variety of semiconductor metal oxides through experiments. The spectrum of the absorption coefficient can be drawn through the reflection spectrum, as shown in Fig. 3b. The absorption coefficient $r_{abs}(\lambda)$ rapidly decreases to below 0.2 at approximately 400 nm, which indicates that the semiconductor

CSTR: 32290.14.JUSTC-2024-0062
DOI: 10.52396/JUSTC-2024-0062
JUSTC, **2025**, 55(2): 0201

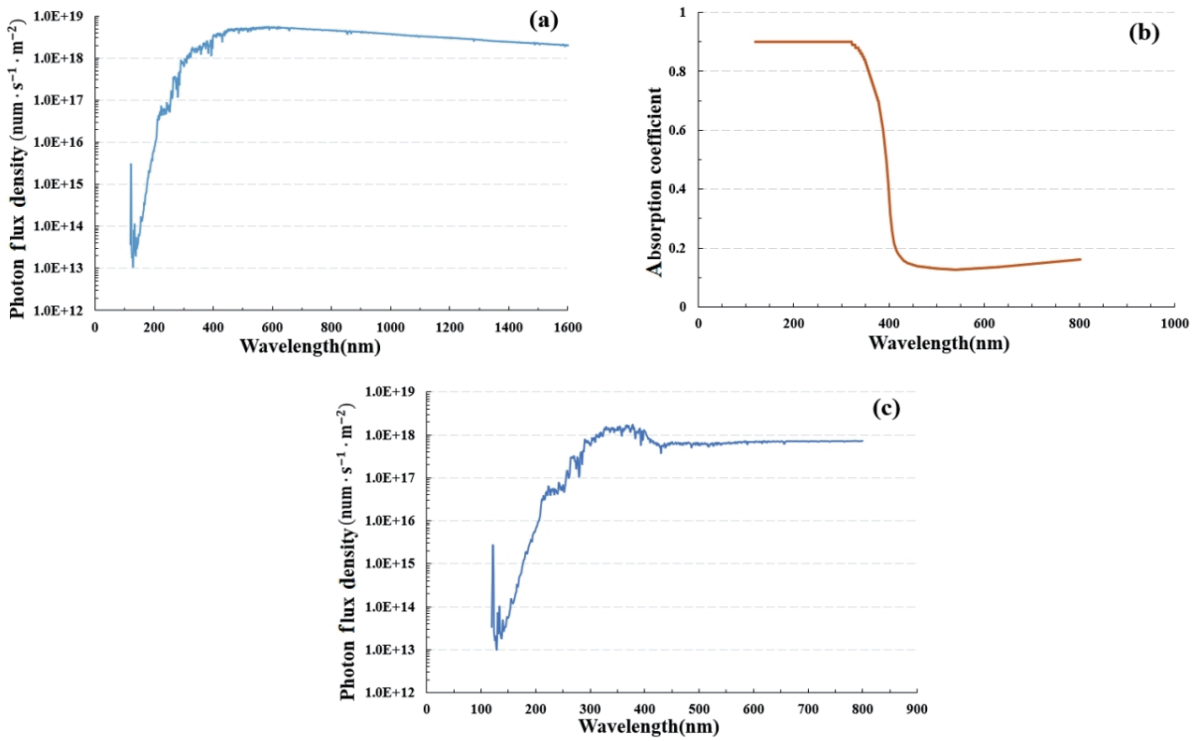

Fig. 3. (a) Solar photon flux density spectrum; (b) spectrum of the absorption coefficient; (c) photon flux density spectrum composed of absorbed photons.

metal oxide material used in this work, i.e., 0.5% Ni-doped TiO_2, should choose the UV band with a wavelength less than 400 nm as the solar radiation band transmitted to the light reaction. Combined with the solar photon flux density spectrum, the photon flux density spectrum composed of absorbed photons ($PFD_{abs}(\lambda)$) can be obtained, as shown in Fig. 3c.

At the same time, only photogenerated electrons that are not combined with holes can participate in the reaction. Therefore, the probability of each photogenerated electron participating in the reaction r_{rea} is the probability that the photogenerated electron–hole pair of the material is not combined, which can be expressed as[28]:

$$r_{rea} = 1 - r_{rec} = \exp\left(\frac{t_{rea}}{t_{EHPs}}\right), \tag{15}$$

where r_{rec} is the recombination rate of photogenerated electron–hole pairs and where t_{rea} and t_{EHPs} are the times required for one elementary reaction and the lifetime of photogenerated carriers, respectively.

Assuming that all successfully separated photogenerated electrons are involved in the formation of oxygen vacancies, the number of effective electrons N_{ee} involved in the formation of oxygen vacancies can be expressed as[29]:

$$N_{ee} = r_{rea} \cdot \min\left\{N_P, S_{lr} t_{lr} \int_{\lambda_1}^{\lambda_2} PFD_{abs}(\lambda)\,d\lambda\right\}. \tag{16}$$

The number of oxygen vacancies formed N_{V_O} can be expressed as:

$$N_{V_O} = \frac{1}{2} N_{ee}. \tag{17}$$

Oxygen molecules generated by oxygen vacancies are adsorbed on the surface of semiconductor metal oxides. Assuming that all the oxygen molecules will be desorbed after a long enough time, the number of generated oxygen molecules N_{O_2} can be expressed as:

$$N_{O_2} = N_{O_2,des} = \frac{1}{2} N_{V_O} = \frac{1}{4} N_{ee}, \tag{18}$$

where $N_{O_2,des}$ is the number of desorbed oxygen molecules.

The next stage is the thermal reaction stage. The solar collector absorbs solar radiation energy greater than the separation wavelength λ_3, that is, the solar radiation energy of band 3 in Fig. 1, and increases the reaction temperature to the temperature T_{tr} required for the thermal reaction. The heat energy Q_{tr} required for this process can be expressed as[29]:

$$Q_{tr} = (T_{tr} - T_0)\left(C_{M_xO_y} M_{M_xO_y} + C_{H_2O} Mol_{H_2O} \frac{U_{H_2O}}{22.4}\right), \tag{19}$$

where T_{tr} and T_0 are the temperatures required for the thermal reaction and ambient temperature, respectively; $C_{M_xO_y}$ and $M_{M_xO_y}$ are the specific heat capacity and mass of the semiconductor metal oxide, respectively; C_{H_2O}, Mol_{H_2O}, and U_{H_2O} are the specific heat capacity, molar mass, and volume of water vapor, respectively; and the volume of water vapor is the volume of the reaction chamber.

The heat Q_{tr} required for the thermal reaction can also be expressed as the product of the solar radiation energy E_{tr} of band 3, the thermal reaction area S_{tr}, and the time t_{tr} required for the thermal reaction, so the time t_{tr} required for the thermal reaction can be expressed as[29]:

CSTR: 32290.14.JUSTC-2024-0062
DOI: 10.52396/JUSTC-2024-0062
JUSTC, **2025**, 55(2): 0201

$$t_{\mathrm{tr}}=\frac{(T_{\mathrm{tr}}-T_0)\left(C_{\mathrm{M_xO_y}}M_{\mathrm{M_xO_y}}+C_{\mathrm{H_2O}}Mol_{\mathrm{H_2O}}\dfrac{U_{\mathrm{H_2O}}}{22.4}\right)}{E_{\mathrm{tr}}S_{\mathrm{tr}}}. \tag{20}$$

When H_2O is introduced into the reaction chamber, H_2O is adsorbed by oxygen vacancies on the surface of semiconductor or metal oxides and reduced to H_2. The generated hydrogen molecules are desorbed after a certain period of time, and the number of hydrogen molecules $N_{\mathrm{H_2}}$ can be expressed as:

$$N_{\mathrm{H_2}}=N_{\mathrm{H_2,des}}=N_{\mathrm{H_2O,ads}}=N_{\mathrm{V_O}}=2N_{\mathrm{O_2}}, \tag{21}$$

where $N_{\mathrm{H_2,des}}$ and $N_{\mathrm{H_2O,ads}}$ are the number of desorbed hydrogen molecules and adsorbed water molecules, respectively.

Finally, the oxygen production rate $\nu_{\mathrm{O_2,pt}}$ and hydrogen production rate $\nu_{\mathrm{H_2,pt}}$ of the photothermal synergistic reaction can be expressed as:

$$\nu_{\mathrm{O_2,pt}}=\frac{N_{\mathrm{O_2}}}{N_{\mathrm{A}}(t_{\mathrm{lr}}+t_{\mathrm{tr}})}, \tag{22}$$

$$\nu_{\mathrm{H_2,pt}}=\frac{N_{\mathrm{H_2}}}{N_{\mathrm{A}}(t_{\mathrm{lr}}+t_{\mathrm{tr}})}, \tag{23}$$

where N_{A} is the Avogadro constant, and its value is taken as 6.022×10^{23}. The specific parameters of the photothermal synergistic reaction are detailed in Table 1.

2.3 Model of the PV/PETE heating section

In this section, the control volume is taken on the basis of the axial length of the cell, and the mass and energy balance equations are established. The impact of momentum balance on performance is negligible[30]. The process of energy transfer and energy balance on a single control volume is shown in Fig. 4. The height and width of the control volume are taken as fixed values, the length is a microelement, and the internal carbon dioxide gas flow temperature is T_{i}.

The solar concentrator gathers sunlight, but owing to optical loss during the gathering process, the system absorbs only a portion of the solar energy, which can be expressed as:

$$\dot{E}_{\mathrm{abs}}(T_{\mathrm{i}})=\dot{E}_{\mathrm{ele}}\cdot\eta_{\mathrm{opt}}, \tag{24}$$

where $\dot{E}_{\mathrm{ele}}$ is the total solar radiation energy. In this work, solar radiation energy is allocated to the electrolytic carbon dioxide component of the full spectrum of solar energy, as shown in Fig. 1, which is the solar radiation energy corresponding to the wave band between wavelengths λ_2 and λ_3. η_{opt} is the optical efficiency. Part of the absorbed solar energy is converted into electric energy through PV cells and the PETE module, and the output electric energy can be expressed as:

$$\dot{W}_{\mathrm{PV}}(T_{\mathrm{i}})=\dot{E}_{\mathrm{abs}}(T_{\mathrm{i}})\cdot\eta_{\mathrm{PV},T_{\mathrm{i}}}, \tag{25}$$

$$\dot{W}_{\mathrm{PETE}}(T_{\mathrm{i}})=\dot{E}_{\mathrm{abs}}(T_{\mathrm{i}})\cdot\eta_{\mathrm{PETE},T_{\mathrm{i}}}, \tag{26}$$

where $\dot{W}_{\mathrm{PV}}(T_{\mathrm{i}})$ and $\dot{W}_{\mathrm{PETE}}(T_{\mathrm{i}})$ are the electrical energy generated by the PV cells and PETE module, respectively, and $\eta_{\mathrm{PV},T_{\mathrm{i}}}$ and $\eta_{\mathrm{PETE},T_{\mathrm{i}}}$ are the photovoltaic efficiencies of the PV cells and PETE module at temperature T_{i}, respectively.

Many kinds of semiconductor materials can be used for PV cells, such as silicon-based semiconductor cells, multicompound thin film cells (CdTe, GaAs, CIGS, etc.), and organic material cells. Different cell materials have different cutoff frequencies and photovoltaic efficiencies. With increasing working temperature, the photovoltaic efficiency of PV cells gradually decreases. Most studies have shown that the applicable temperature range of PV cells is no more than 250 °C. In this work, quadruple-junction GaAs PV cells are used as power generation and waste heat recovery devices at low temperatures (below 250 °C), and the power generation efficiency of the PV cells can be expressed as follows[31]:

$$\eta_{\mathrm{PV},T_{\mathrm{i}}}=\eta_{\mathrm{cell},T_{\mathrm{i}}}\cdot\eta_{\mathrm{mod}}, \tag{27}$$

where $\eta_{\mathrm{cell},T_{\mathrm{i}}}$ is the photovoltaic efficiency of multijunction GaAs PV cells and η_{mod} is the module efficiency (defined as the ratio of the PV module efficiency to the PV cell efficiency), which is 0.9. When the temperature is T_{i}, the

Table 1. Specific parameters of the photothermal synergistic reaction section.

Parameters	Symbol (unit)	Value
Area of solar radiation absorbed in the light reaction	$S_{\mathrm{lr}}\left(\mathrm{m^2}\right)$	1
Time taken for the light reaction	t_{lr} (s)	3600[29]
Time required for one elementary reaction	t_{rea} (ns)	1[28]
Lifetime of photogenerated carriers	t_{EHPs} (ns)	6.028[28]
Temperature required for thermal reaction	T_{tr} (K)	773.15[29]
Ambient temperature	T_0 (K)	298.15[29]
Specific heat capacity of semiconductor metal oxide	$C_{\mathrm{M_xO_y}}$ (J/(g·K))	0.71
Mass of semiconductor metal oxide	$M_{\mathrm{M_xO_y}}$ (g)	25.45
Specific heat capacity of water vapor	$C_{\mathrm{H_2O}}$(J/(g·K))	1.978
Molar mass of water vapor	$Mol_{\mathrm{H_2O}}$	18
Volume of water vapor	$U_{\mathrm{H_2O}}\left(\mathrm{m^3}\right)$	0.1
Area of thermal reaction	$S_{\mathrm{tr}}\left(\mathrm{m^2}\right)$	1

CSTR: 32290.14.JUSTC-2024-0062
DOI: 10.52396/JUSTC-2024-0062
JUSTC, **2025**, 55(2): 0201

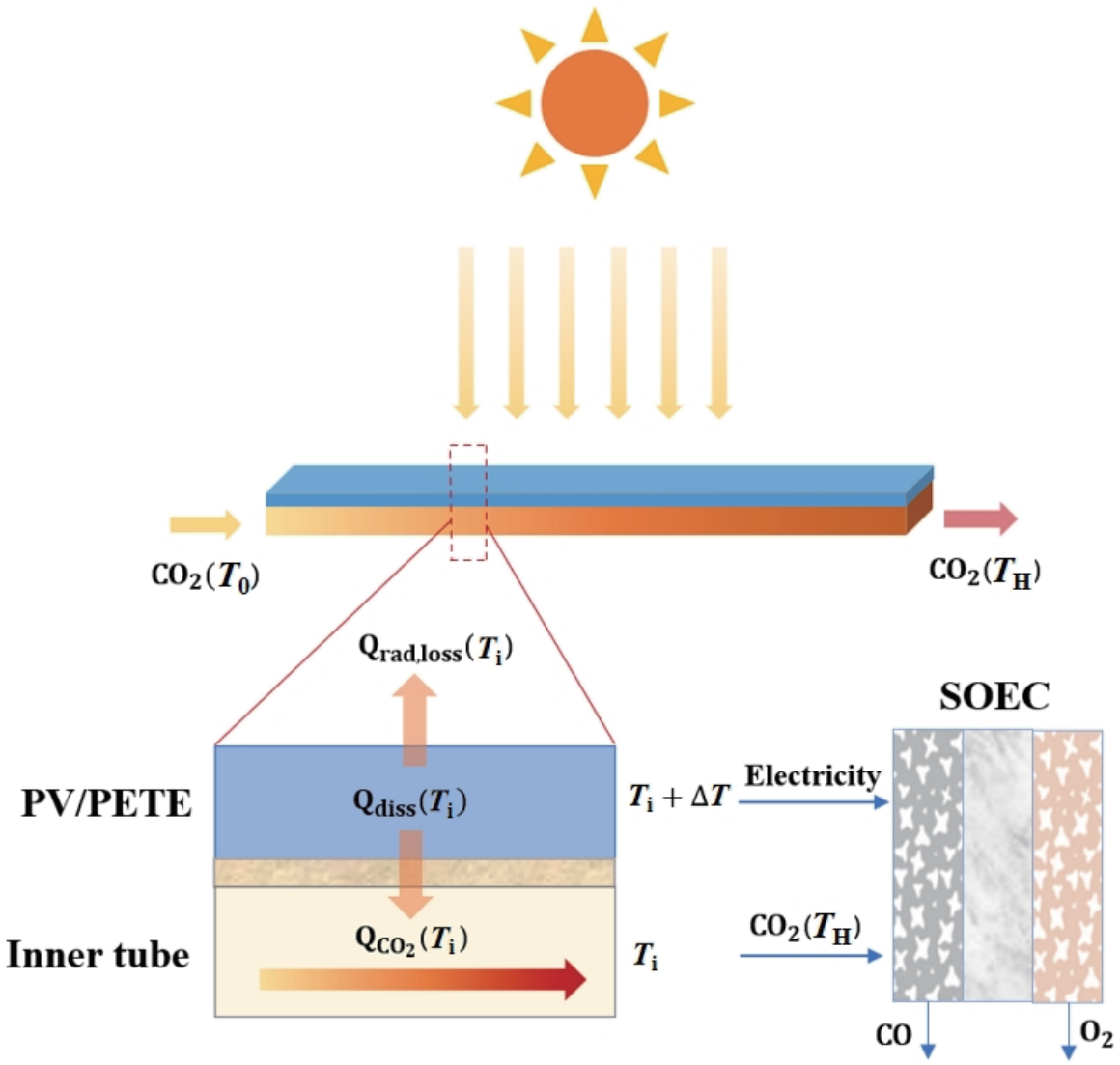

Fig. 4. Schematic diagram of the energy analysis for the PV/PETE heating section.

efficiency of multijunction GaAs PV cells is expressed as[32]:

$$\eta_{\mathrm{cell},T_i} = \eta_{0,T_i} + 0.0142\ln C + \left(-0.000715 + 6.97\times10^{-5}\ln C\right)\times(T_i + \Delta T - T_0), \quad (28)$$

where η_{0,T_i} is the photovoltaic efficiency of multijunction GaAs PV cells at 25 °C, and the photovoltaic efficiency of the quadruple-junction GaAs PV cells in this work can be taken as 37.2%[32]. C represents the aggregation ratio of the solar collector; ΔT represents the heat transfer temperature difference between the PV cell and the carbon dioxide flow, taken as 10 °C; and T_0 represents the ambient temperature.

Correspondingly, the PETE module serves as a power generation and waste heat recovery device at high temperatures (above 250 °C). The PETE module requires a high solar concentration to obtain high temperatures, and the photovoltaic conversion efficiency can reach 32% and 47% at concentrations of 100 and 3000 times, respectively[33]. The photovoltaic efficiency of the PETE module is related to the operating temperature and the electron affinity χ on the cathode surface. In this work, the highest photovoltaic efficiency at different χ values is taken as the photovoltaic efficiency of the PETE module, as shown by the full line in Fig. 5. The photovoltaic efficiency at different cathode surface electron affinities χ is as follows[23]:

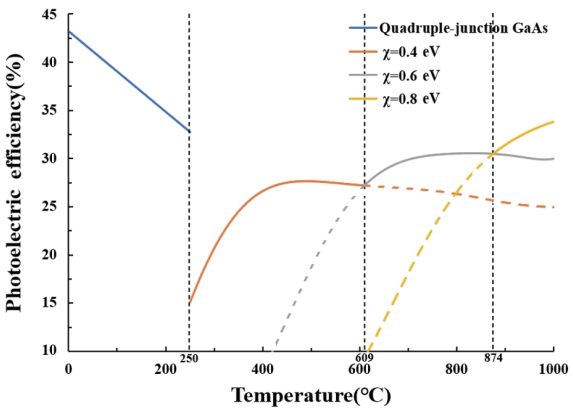

Fig. 5. The photovoltaic efficiency of the quadruple-junction GaAs and PETE module as a function of temperature for the proposed system.

CSTR: 32290.14.JUSTC-2024-0062
DOI: 10.52396/JUSTC-2024-0062
JUSTC, **2025**, 55(2): 0201

$$\begin{aligned}\eta_{\mathrm{PETE},T_\mathrm{i}} =& 0.41163-9.3412\times10^{-3}T_\mathrm{i}+7.3927\times10^{-5}T_\mathrm{i}^2-2.5151\times\\ & 10^{-7}T_\mathrm{i}^3+4.5432\times10^{-10}T_\mathrm{i}^4-4.5639\times10^{-13}T_\mathrm{i}^5+\\ & 2.4116\times10^{-16}T_\mathrm{i}^6-5.2328\times10^{-20}T_\mathrm{i}^7,\ \chi=0.4\ \mathrm{eV};\\ \eta_{\mathrm{PETE},T_\mathrm{i}} =& -2.38144+3.7360\times10^{-2}T_\mathrm{i}-2.34382\times10^{-4}T_\mathrm{i}^2+7.561\times\\ & 10^{-7}T_\mathrm{i}^3-1.35138\times10^{-9}T_\mathrm{i}^4+1.36022\times10^{-12}T_\mathrm{i}^5-\\ & 7.2428\times10^{-16}T_\mathrm{i}^6+1.5904\times10^{-19}T_\mathrm{i}^7,\ \chi=0.6\ \mathrm{eV};\\ \eta_{\mathrm{PETE},T_\mathrm{i}} =& -9.4176+8.8734\times10^{-2}T_\mathrm{i}-3.3662\times10^{-4}T_\mathrm{i}^2+6.5628\times\\ & 10^{-7}T_\mathrm{i}^3-6.9475\times10^{-10}T_\mathrm{i}^4+3.8473\times10^{-13}T_\mathrm{i}^5-\\ & 9.1502\times10^{-17}T_\mathrm{i}^6+2.884\times10^{-21}T_\mathrm{i}^7,\ \chi=0.8\ \mathrm{eV}.\end{aligned} \tag{29}$$

The solar radiation energy absorbed by the system, with the exception of the part used to generate electrical energy, is collected and used to heat the carbon dioxide flowing in the pipeline. Therefore, the thermal energy supplied to the system is solar radiation energy that is not converted into electrical energy, which is expressed as:

$$\dot{Q}_{\mathrm{diss}}(T_\mathrm{i})=\begin{cases}\dot{E}_{\mathrm{abs}}(T_\mathrm{i})\cdot(1-\eta_{\mathrm{PV},T_\mathrm{i}}),\ \text{PV cells};\\ \dot{E}_{\mathrm{abs}}(T_\mathrm{i})\cdot(1-\eta_{\mathrm{PETE},T_\mathrm{i}}),\ \text{PETE module}.\end{cases} \tag{30}$$

When carbon dioxide is heated, there is usually a loss of convection and radiation heat transfer. However, owing to the vacuum environment on the lunar surface, convective heat transfer does not occur, so only radiation heat transfer is considered. A silver-plated heat shield is installed on the outer wall of the equipment to prevent radiation heat transfer with the sky and only with the ground. The amount of radiation heat loss is shown as follows[23]:

$$\dot{Q}_{\mathrm{rad,loss}}(T_\mathrm{i})=\varepsilon_0\cdot\sigma\cdot\mathrm{d}A\cdot\left(T_\mathrm{i}^4-T_{\mathrm{gro}}^4\right), \tag{31}$$

where A is the area of solar energy received by the PV cells and PETE module; ε_0 is the emissivity of the absorption layer; σ is the Stefan–Boltzmann constant, which is taken as 5.67×10^{-8} W/(m^2·K^4); and T_{gro} is the ground temperature. The heat absorbed by the carbon dioxide flow is the residual heat recovered by the system minus the radiation loss of heat. The heat absorbed by carbon dioxide in each control volume can be expressed as[23]:

$$\dot{Q}_{\mathrm{CO_2}}(T_\mathrm{i})=\dot{Q}_{\mathrm{diss}}(T_\mathrm{i})-\dot{Q}_{\mathrm{rad,loss}}(T_\mathrm{i})=\dot{n}_{\mathrm{CO_2}}\cdot\int_{T_\mathrm{i}}^{T_{\mathrm{i+1}}}C_{\mathrm{p,CO_2},T_\mathrm{i}}\mathrm{d}T, \tag{32}$$

where $\dot{n}_{\mathrm{CO_2}}$ is the molar flow rate of carbon dioxide and where $C_{\mathrm{p,CO_2},T_\mathrm{i}}$ is the constant pressure specific heat capacity of carbon dioxide at temperature T_i. The specific parameters of the PV/PETE heating section are detailed in Table 2.

2.4 Model of the electrolysis section

At a specific temperature and gas concentration, the Nernst equation can be used to predict the minimum potential required for the electrolysis of carbon dioxide, that is, the equilibrium potential V_{equ}, which can be expressed as[34]:

$$V_{\mathrm{equ}}=V_0+\frac{\mathrm{R}T_\mathrm{e}}{2F}\ln\left[\frac{P_{\mathrm{CO}}^0\left(P_{\mathrm{O_2}}^0\right)^{0.5}}{P_{\mathrm{CO_2}}^0}\right], \tag{33}$$

where R is the ideal gas constant, and its value is 8.3145 J·mol^{-1}·K^{-1}; T_e is the temperature of carbon dioxide entering the SOEC after heating by PV/PETE modules; F is the Faraday constant, and its value is 96485 C·mol^{-1}; P_{CO}^0, $P_{\mathrm{O_2}}^0$, and $P_{\mathrm{CO_2}}^0$ represent the partial pressures of CO, O_2, and CO_2 on the electrode surface, respectively; and V_0 is the equilibrium potential under standard pressure. The temperature range of 800–1200 K can be approximately expressed via the following formula[35]:

$$V_0=1.1043-0.00045(T_\mathrm{e}-800). \tag{34}$$

In fact, during SOEC operation, the required cell potential V is always greater than the equilibrium potential V_{equ} because some overpotential φ is generated during electrolysis to overcome the irreversibility caused by reactant and product transport, charge transfer and resistance of the electrolyte and electrode. The overpotential φ mainly includes the activation overpotential φ_{act}, concentration overpotential φ_{con}, and ohmic overpotential φ_{ohm}, which are calculated and analyzed below.

2.4.1 Activation overpotential φ_{act}

The activation overpotential of the electrode is the additional voltage required for the electrolytic carbon dioxide reaction due to polarization. The magnitude of the overpotential is affected by the physical conditions and reaction conditions in the electrolysis process, including the reaction location, the temperature of the electrolytic cell, the morphology of the cathode and anode, and the characteristics of the catalytic materials. According to the Butler–Voulmer equation, the activation overpotential of the electrode $\varphi_{\mathrm{act},k}$ can be expressed as[36]:

$$\varphi_{\mathrm{act},k}=\frac{\mathrm{R}T_\mathrm{e}}{F}\cdot\ln\left(\frac{J}{2J_{0,k}}+\sqrt{1+\left(\frac{J}{2J_{0,k}}\right)^2}\right), \tag{35}$$

where the subscript k = a represents the anode and k = c represents the cathode; J represents the current density of the SOEC; and $J_{0,k}$ represents the exchange current density, which is defined as the two-way flow current per unit area when the electrode reaction reaches equilibrium and can be calculated from the following formula[36]:

$$J_{0,k}=\gamma_k\cdot\exp\left(\frac{-E_{\mathrm{act},k}}{\mathrm{R}T_\mathrm{e}}\right), \tag{36}$$

where γ_k is the preexponential factor of the anode or cathode

Table 2. Specific parameters of the PV/PETE heating section.

Parameters	Symbol (unit)	Value
Optical efficiency	η_{opt}	0.73[23]
Module efficiency	η_{mod}	0.9[23]
Heat transfer temperature difference	ΔT (K)	10
Ambient temperature	T_0 (K)	298.15
Length of heating section	L (m)	3
Width of heating section	W (m)	0.1
Height of heating section	H (m)	0.001
Light receiving area	$A\left(\mathrm{m}^2\right)$	0.3
Emissivity of the absorption layer	ε_0	0.1[23]

CSTR: 32290.14.JUSTC-2024-0062
DOI: 10.52396/JUSTC-2024-0062
JUSTC, 2025, 55(2): 0201

and $E_{act,k}$ is the activation energy level at the anode or cathode.

2.4.2 Concentration overpotential φ_{con}

The concentration overpotential is caused by the resistance to the transport of reactants close to the reaction site and products leaving the reaction site. According to previous studies on SOEC electrolysis of H_2O, by replacing H_2O and H_2 with CO_2 and CO, the cathodic concentration overpotential $\varphi_{con,c}$ of the SOEC for CO_2 electrolysis can be obtained as follows[37]:

$$\varphi_{con,c} = \frac{RT_e}{2F} \cdot \ln\left(\frac{1 + RT_e JL_c/(2FD^{eff}_{CO}P^0_{CO})}{1 - RT_e JL_c/\left(2FD^{eff}_{CO_2}P^0_{CO_2}\right)}\right), \tag{37}$$

where L_c is the thickness of the cathode, D^{eff}_{CO} and $D^{eff}_{CO_2}$ represent the effective diffusion coefficients of CO and CO_2, respectively, which can be calculated via the following formula[37]:

$$\frac{1}{D^{eff}_{CO}} = \left(\frac{1}{D^{eff}_{CO,Kn}} + \frac{1}{D^{eff}_{CO_2-CO}}\right) = \frac{\xi}{\varepsilon}\left(\frac{1}{D_{CO,Kn}} + \frac{1}{D_{CO_2-CO}}\right), \tag{38}$$

$$\frac{1}{D^{eff}_{CO_2}} = \left(\frac{1}{D^{eff}_{CO_2,Kn}} + \frac{1}{D^{eff}_{CO_2-CO}}\right) = \frac{\xi}{\varepsilon}\left(\frac{1}{D_{CO_2,Kn}} + \frac{1}{D_{CO_2-CO}}\right), \tag{39}$$

where ξ/ε is the ratio of electrode tortuosity to porosity; $D_{CO,Kn}$ and $D_{CO_2,Kn}$ are the Knudsen diffusion coefficients of CO and CO_2, respectively; and D_{CO_2-CO} is the molecular diffusion coefficient for the CO_2–CO binary system. The Knudsen diffusion coefficients ($D_{CO,Kn}$ and $D_{CO_2,Kn}$) and the molecular diffusion coefficient (D_{CO_2-CO}) can be calculated as follows[37]:

$$D_{CO,Kn} = \frac{2r}{3}\sqrt{\frac{8RT_e}{\pi M_{CO}}}, \tag{40}$$

$$D_{CO_2,Kn} = \frac{2r}{3}\sqrt{\frac{8RT_e}{\pi M_{CO_2}}}, \tag{41}$$

$$D_{CO_2-CO} = \frac{0.0026T_e^{1.5}}{PM^{0.5}_{CO_2-CO}\sigma^2_{CO_2,CO}\Omega_D}, \tag{42}$$

where r is the mean pore radius; M_{CO} and M_{CO_2} are the relative molecular weights of CO and CO_2, respectively; P is the working pressure, whose value is standard atmospheric pressure; M_{CO_2-CO} is the harmonic mean of M_{CO} and M_{CO_2}, i.e., $M_{CO_2-CO} = 2/[(1/M_{CO}) + (1/M_{CO_2})]$; $\sigma_{CO_2,CO}$ is the average characteristic length of CO and CO_2; and Ω_D is the dimensionless diffusion collision integral. $\sigma_{CO_2,CO}$ and Ω_D can be calculated via the following formulas[38]:

$$\sigma_{CO_2,CO} = \frac{\sigma_{CO_2} + \sigma_{CO}}{2}, \tag{43}$$

$$\Omega_D = \frac{1.06036}{\tau^{0.1561}} + \frac{0.193}{\exp(0.47625\tau)} + \frac{1.03587}{\exp(1.52996\tau)} + \frac{1.76474}{3.89411\tau}, \tag{44}$$

where τ is the dimensionless temperature of the CO_2 and CO binary system, which can be obtained from the following formula[38]:

$$\tau = \frac{k_b T_e}{\varepsilon_{i,j}}, \tag{45}$$

where k_b is Boltzmann's constant, and its value is 1.38066×10^{-23} J/K; $\varepsilon_{i,j}$ is the characteristic length, which can be expressed as $\varepsilon_{i,j} = (\varepsilon_i\varepsilon_j)^{1/2}$. The values of σ_{CO}, σ_{CO_2}, and ε_i/k_b are shown in Table 3[38].

At the anode, oxygen is the only gas generated on the porous electrode. The flow of oxygen is determined by Darcy's law. The concentration overpotential of the anode $\varphi_{con,a}$ can be obtained through previous studies and is expressed as[39]:

$$\varphi_{con,a} = \frac{RT_e}{4F}\ln\left[\frac{\sqrt{\left(P^0_{O_2}\right)^2 + JRT_e\mu L_a/(2FB_g)}}{P^0_{O_2}}\right], \tag{46}$$

where μ is the dynamic viscosity of oxygen; L_a is the thickness of the anode; and B_g is the permeability of the anode, which can be calculated via the following formula[39]:

$$B_g = \frac{r^2\varepsilon^3}{[18\xi(1-\varepsilon)^2]}. \tag{47}$$

2.4.3 Ohmic overpotential φ_{ohm}

The ohmic overpotential is generated mainly by the conduction resistance of ions through the electrolyte and electrons through the electrode. According to Ohm's law, the ohmic overpotential φ_{ohm} can be expressed as[39]:

$$\varphi_{ohm} = JR_{ohm} = J\left(\frac{L_a}{\sigma_a} + \frac{L_c}{\sigma_c} + \frac{L_e}{\sigma_e}\right), \tag{48}$$

where L_e is the thickness of the electrolyte and σ_c, σ_a, and σ_e are the conductivities of the cathode, anode and electrolyte, respectively. To facilitate calculation, the conductivities of the cathode and anode are taken as constants, whereas the conductivity of the electrolyte is a function of the working temperature.

Thus far, the total potential V required for the electrolysis of a carbon dioxide SOEC can be obtained, that is, the sum of the equilibrium potential and each overpotential, as follows:

$$V = V_{equ} + \varphi_{act,c} + \varphi_{act,a} + \varphi_{con,c} + \varphi_{con,a} + \varphi_{ohm}. \tag{49}$$

According to Faraday's law, the rate of CO $\nu_{CO,e}$ formation from the SOEC cathode can be expressed as:

$$\nu_{CO,e} = \frac{JA_e}{2F}, \tag{50}$$

where A_e is the surface area of the SOEC. Moreover, according to the chemical formula of carbon dioxide electrolysis, the

Table 3. Parameters for calculating the dimensionless diffusion collision integrals[38].

	CO	CO_2
σ_i	3.690	3.941
ε_i/k_b	91.700	195.200

CSTR: 32290.14.JUSTC-2024-0062
DOI: 10.52396/JUSTC-2024-0062
JUSTC, **2025**, 55(2): 0201

generation rate of anode oxygen $v_{O_2,e}$ can be obtained as follows:

$$v_{O_2,e} = \frac{1}{2} v_{CO,e}. \tag{51}$$

The specific parameters of the electrolysis section are detailed in Table 4.

2.5 Comprehensive oxygen production model

Through the establishment and analysis of models of oxygen production by photothermal synergistic reactions and electrolytic carbon dioxide, the total oxygen production rate v_{O_2} of the comprehensive model can be obtained as follows:

$$v_{O_2} = v_{O_2,pt} + v_{O_2,e}. \tag{52}$$

3 Model validation

In this section, the accuracy of the photothermal synergistic reaction module, PV/PETE heating module, and electrolytic carbon dioxide module in the process of model establishment is verified through other studies.

3.1 Model validation of the synergistic photothermal reaction

The photocatalytic material used in the photothermal synergistic reaction model in this paper is 0.5% Ni-doped TiO_2. According to reports in Ref. [40], the oxygen production rate of 0.5% Ni-doped TiO_2 is 60 μmol·h^{-1}. A comparison between the results of this model and those of Ref. [40] when the same material is used for simulation is shown in Fig. 6.

Table 4. Specific parameters of the electrolysis section.[①]

Parameters	Symbol (unit)	Value
Operating pressure	P (Pa)	10^5
Cathode surface gas composition	—	30 mol% CO/ 70 mol% CO_2
Cathode preexponential factor	$\gamma_c\left(A\cdot m^{-2}\right)$	1.344×10^{10}[39]
Anode preexponential factor	$\gamma_a\left(A\cdot m^{-2}\right)$	2.051×10^{9}[39]
Activation energy for cathode	$E_{act,c}\left(J\cdot mol^{-1}\right)$	1.0×10^{5}[39]
Activation energy for anode	$E_{act,a}\left(J\cdot mol^{-1}\right)$	1.2×10^{5}[39]
Cathode thickness	L_c (m)	5.0×10^{-5}[39]
Electrolyte thickness	L_e (m)	5.0×10^{-5}[39]
Anode thickness	L_a (m)	5.0×10^{-4}[39]
Electrode tortuosity	ξ	5.0[39]
Electrode porosity	ε	0.4[39]
Mean pore radius	r (m)	5.0×10^{-5}[39]
Relative molecular weights of CO	M_{CO}	28
Relative molecular weights of CO_2	M_{CO_2}	44
Conductivities of anode	$\sigma_a(\Omega^{-1}\cdot m^{-1})$	8.4×10^{3}[39]
Conductivities of cathode	$\sigma_c(\Omega^{-1}\cdot m^{-1})$	8.0×10^{4}[39]
Conductivities of electrolyte	$\sigma_e(\Omega^{-1}\cdot m^{-1})$	$3.34\times10^{4}\cdot\exp(-1.03\times10^{4}/T)$[39]
Surface area of SOEC	$A_e\left(m^2\right)$	6.4×10^{-3}

Fig. 6 shows not only the comparison between this model and Ref. [40] when 0.5% Ni-doped TiO_2 was used but also the oxygen production rate when different amounts of Ni were doped on the TiO_2 substrate. These findings indicate that the 0.5% Ni-doped TiO_2 selected in this study has a relatively high oxygen production rate. Fig. 6 shows that for the same material, the oxygen production rate of the photothermal synergistic reaction model in this work is 62.15 μmol·h^{-1}, which is 2.15 μmol·h^{-1} higher than the reference value[40], and the relative error is 3.58%, which is within the allowable error range of 5%. This proves that the photothermal synergistic reaction model in this work has high accuracy.

3.2 Model validation of the PV/PETE heating section

Wang et al.[23] established a model of the relationship between the PV/PETE water/steam flow temperature and the flow rate and tube length and obtained simulation results. Under the conditions of the same parameters and with the exchange water as the flow and heat transfer medium, the simulation results are also obtained by using the PV/PETE model established in this paper, as shown in Fig. 7.

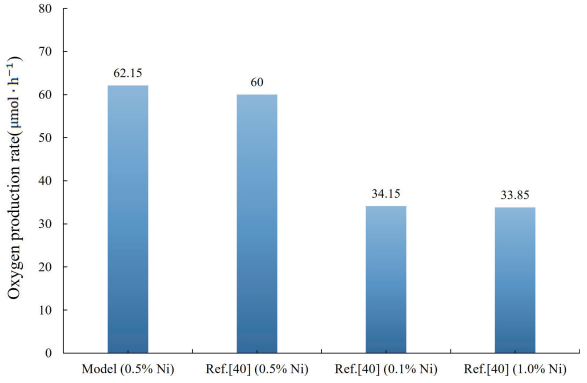

Fig. 6. Comparison of the simulation results of the oxygen production rate of the synergistic photothermal reaction between this model and Ref. [40].

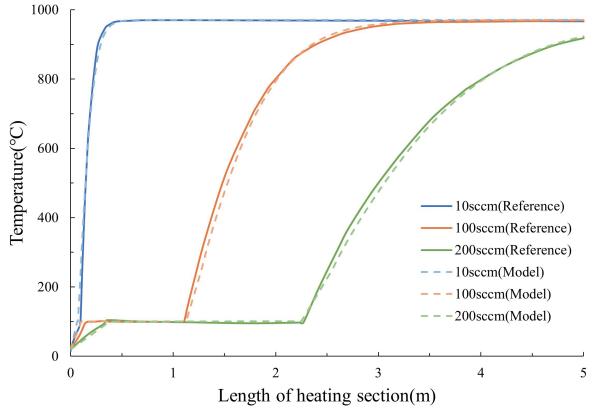

Fig. 7. Variation in the PV/PETE temperature with the flow rate and tube length in this model and Ref. [23].

[①] Structural and physical parameters of electrolysis cells are set as a typical configuration of Ref. [39], since the purpose of this paper is to investigate the CO_2 electrolysis rate, rather than the design and optimization of the cell structure.

CSTR: 32290.14.JUSTC-2024-0062
DOI: 10.52396/JUSTC-2024-0062
JUSTC, **2025**, 55(2): 0201

Fig. 7 takes three typical flow rates as representatives to compare the simulation results of the model in this paper with those in Ref. [23]. There is a straight line segment with a constant temperature in the curve, which is caused by the latent heat of the water phase change. The results of the model in this paper are in good agreement with those in Ref. [23]. In the case of three different flow rates, the maximum errors of the two temperatures at any length of the tube are 14.6 °C, 36.5 °C, and 29.1 °C, and the maximum relative errors are 1.51%, 3.76%, and 3.00%, respectively, which are within the allowable error range of 5%, which proves that the model in this paper has high accuracy.

3.3 Model validation of the electrolysis section

Ebbesen et al.[41] experimentally determined the relationship between the total potential V and current density J of a SOEC for the electrolysis of carbon dioxide. The experiment was carried out at a temperature of 1123 K, the thicknesses of the anode layer, cathode layer, and electrolyte layer were 17.5 μm, 312.5 μm, and 12.5 μm, respectively, and the gas composition of the cathode was 70% CO_2 and 30% CO. In this work, the electrolysis model was adjusted according to the parameters of this reference and simulated. The comparison between the simulation results of this model and the reference is shown in Fig. 8.

Fig. 8 shows that the simulation results of the model in this paper maintain high similarity with Ref. [41]. With increasing current density, the total potential V of the SOEC increases. The maximum error between the simulation results of this model and the reference model is 0.021 V, and the maximum relative error is 1.67%, which is within the allowable range of 5%, indicating that this model has high accuracy.

4 Results and discussion

In this chapter, the oxygen production rate of the integrated oxygen production model is comprehensively displayed, and the effects of the electrolysis temperature, different UV and IR separation wavelengths, and different photovoltaic materials on the oxygen production rate are discussed.

The photovoltaic material used in this work is quadruple-junction GaAs, and the semiconductor metal oxide material used in the photothermal synergistic reaction is 0.5% Ni-doped TiO_2. The solar radiation transmitted to the light reaction, heating and electrolysis module, and thermal reaction is the solar radiation corresponding to band 1, band 2, and band 3, respectively.

4.1 Effect of electrolysis temperature on the oxygen production rate

This section explores the effect of the carbon dioxide electrolysis temperature on the oxygen production rate in an SOEC, keeping the UV separation wavelength $\lambda_2 = 400$ nm and the IR separation wavelength $\lambda_3 = 900$ nm unchanged. The temperature T_e of the carbon dioxide entering the SOEC is determined by the PV/PETE module, but there are two different situations in the PV/PETE module. First, when the flow rate of carbon dioxide is low, carbon dioxide is heated until the provided heat, carbon dioxide heat absorption, radiation and convection heat dissipation are balanced, and then the carbon dioxide that reaches the equilibrium temperature flows out of the heating module. In the second case, when the flow of carbon dioxide is high, the heat balance is not reached until the carbon dioxide flows out of the heating module, so the temperature of the outgoing carbon dioxide is lower than the equilibrium temperature.

An adult exhales carbon dioxide at a rate of approximately 22.6 L/h, which is recorded as a unit of carbon dioxide. Fig. 9 shows the temperature changes of different units of carbon dioxide after they enter the PV/PETE module. The figure shows that 10, 100, and 500 units of carbon dioxide reach thermal equilibrium when leaving the heating module, and the temperature at this time is approximately 1235 K. However, 1000 units and 2000 units of carbon dioxide did not reach the thermal balance, which indicates that when the carbon dioxide flow reached a certain level, the temperature of the carbon dioxide entering the SOEC decreased. We further studied the influence of temperature on the effect of carbon dioxide electrolysis, thereby affecting the oxygen production rate. The maximum temperature was 1235 K, and a temperature of 25 K was used to analyze the oxygen production rate of the comprehensive model at different temperatures, as shown in Fig. 10. The specific values of the oxygen production rate at different temperatures are listed in Table 5. The data in the

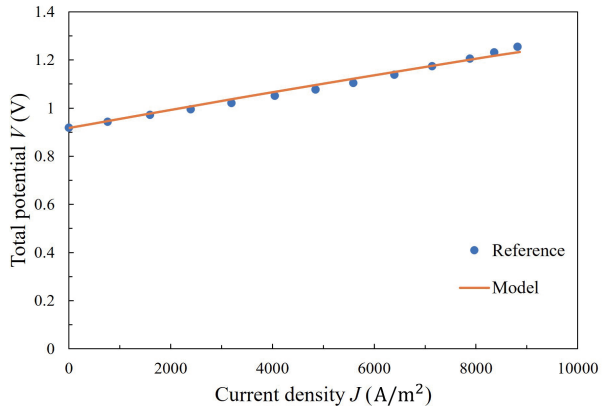

Fig. 8. Comparison of the total potential of the SOEC between the simulation results and reference results at different current densities.

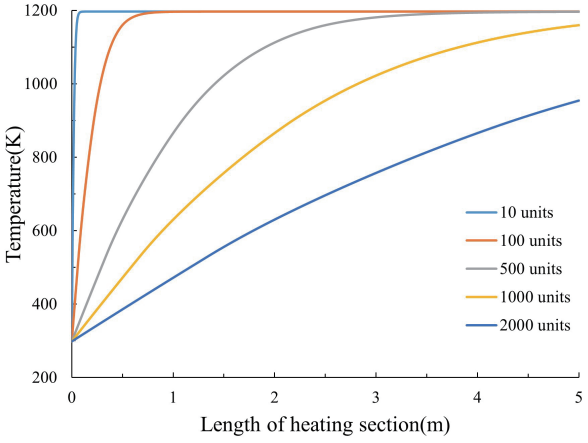

Fig. 9. Temperature changes of different units of carbon dioxide flow in the PV/PETE module.

CSTR: 32290.14.JUSTC-2024-0062
DOI: 10.52396/JUSTC-2024-0062
JUSTC, **2025**, 55(2): 0201

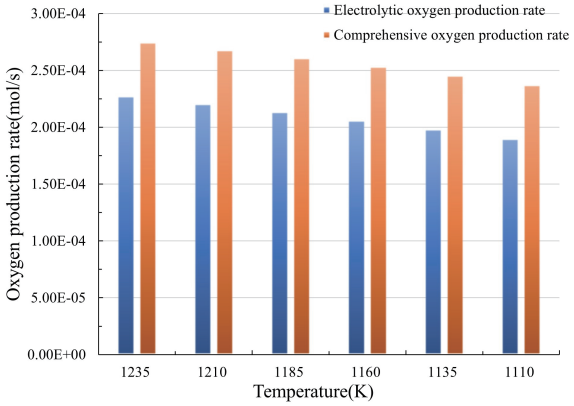

Fig. 10. Electrolytic oxygen production rate and comprehensive oxygen production rate at different carbon dioxide temperatures in the SOEC.

Table 5. Specific values of the oxygen production rate at different temperatures.

Temperature of carbon dioxide T_e (K)	Electrolytic oxygen production rate $v_{O_2,e}$ (mol/s)	Comprehensive oxygen production rate v_{O_2} (mol/s)
1235	2.2715×10^{-4}	2.7447×10^{-4}
1210	2.2051×10^{-4}	2.6783×10^{-4}
1185	2.1345×10^{-4}	2.6076×10^{-4}
1160	2.0594×10^{-4}	2.5326×10^{-4}
1135	1.9800×10^{-4}	2.4532×10^{-4}
1110	1.8964×10^{-4}	2.3696×10^{-4}

figure and table indicate that the highest electrolytic oxygen production rate and comprehensive oxygen production rate can be achieved at 1235 K, which are 2.2715×10^{-4} mol/s and 2.7447×10^{-4} mol/s, respectively. With the decrease in the temperature of carbon dioxide entering the SOEC, both the oxygen production rate of electrolytic carbon dioxide and the comprehensive oxygen production rate decrease. This is because the calculation of each potential in the electrolysis process involves the temperature. As the temperature decreases, the total potential increases. When the total solar radiation supplied to the electrolysis and heating module remains unchanged, the current density decreases, which leads to a decrease in the oxygen production rate. Therefore, if conditions permit, the temperature at which carbon dioxide enters the SOEC should be increased as much as possible to obtain a higher oxygen production rate. For the model in this paper, owing to the limited number of people in the lunar human base, the actual carbon dioxide flow cannot reach the level that makes its temperature lower than the thermal equilibrium temperature, so the carbon dioxide entering the SOEC can be kept at the thermal equilibrium temperature in general.

4.2 Effect of the UV separation wavelength λ_2 on the oxygen production rate

This section explores the effects of the UV separation wavelength λ_2 on the oxygen production rate, keeping the IR separation wavelength $\lambda_3 = 900$ nm and electrolysis temperature $T_e = 1235$ K unchanged. The UV separation wavelength λ_2 affects the solar radiation delivered to the light reaction and heating electrolysis module. Within the allowable range of λ_2, when λ_2 decreases, the solar radiation energy allocated to the light reaction decreases, which reduces the number of oxygen vacancies N_{V_O} generated by the light reaction and reduces the oxygen production rate of the synergistic photothermal reaction. However, a decrease in λ_2 increases the amount of solar radiation energy allocated to the heating electrolytic module and then increases the rate of oxygen production from electrolytic carbon dioxide. Therefore, this section explores the changes in the comprehensive oxygen production rate of this model at different UV separation wavelengths λ_2 (400 nm, 395 nm, 390 nm, 385 nm, 380 nm, 375 nm, 370 nm, 365 nm, and 360 nm) when the IR separation wavelength $\lambda_3 = 900$ nm and explores the optimal UV separation wavelength, as shown in Fig. 11.

As shown in Fig. 11a, with decreasing UV separation wavelength λ_2, the oxygen production rate $v_{O_2,pt}$ of the synergistic photothermal reaction decreases, and the oxygen production rate $v_{O_2,e}$ of electrolytic carbon dioxide increases. Fig. 11b shows that with decreasing UV separation wavelength λ_2, the comprehensive oxygen production rate v_{O_2} first increases but then decreases. The UV separation wavelength λ_2 reaches the maximum oxygen production rate at 385 nm, with a value of 2.7545×10^{-4} mol/s. Therefore, when the UV separation wavelength λ_2 is greater than 385 nm, reducing the separation wavelength has a greater impact on the increase in the oxygen production rate $v_{O_2,e}$ of electrolytic carbon dioxide. When the UV separation wavelength λ_2 is less than 385 nm, the reduction in the separation

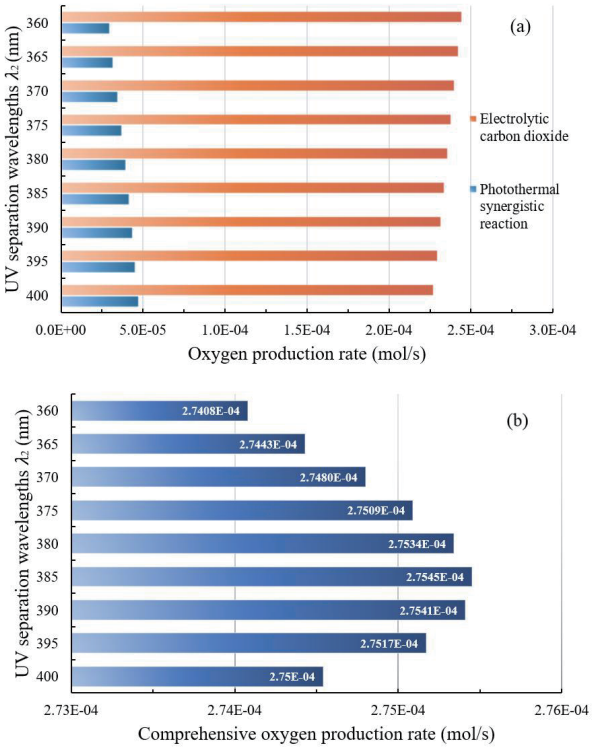

Fig. 11. (a) Oxygen production rates of the synergistic photothermal and electrolytic carbon dioxide reactions at different UV separation wavelengths. (b) Comprehensive oxygen production rates at different UV separation wavelengths.

CSTR: 32290.14.JUSTC-2024-0062
DOI: 10.52396/JUSTC-2024-0062
JUSTC, **2025**, 55(2): 0201

wavelength has a greater effect on the reduction in the oxygen production rate $v_{O_2,pt}$ of the synergistic photothermal reaction. To ensure that the comprehensive model reaches the highest comprehensive oxygen production rate v_{O_2}, the UV separation wavelength λ_2 should be approximately 385 nm. The specific data are listed in Table 6.

4.3 Effect of the IR separation wavelength λ_3 on the oxygen production rate

This section explores the effects of the IR separation wavelength λ_3 on the oxygen production rate, keeping the UV separation wavelength λ_2 = 385 nm and electrolysis temperature T_e = 1235 K unchanged. The IR separation wavelength λ_3 affects the solar radiation energy transferred to the heating electrolytic module and the thermal reaction. Within the allowable range of the IR separation wavelength λ_3, when λ_3 decreases, the solar radiation energy allocated to the heating electrolytic module decreases, and the oxygen production rate of electrolytic carbon dioxide decreases. However, a decrease in λ_3 increases the amount of solar radiation energy allocated to the thermal reaction, which reduces the time t_{tr} required for the thermal reaction and then increases the oxygen production rate of the synergistic photothermal reaction. Therefore, this section discusses the changes in the comprehensive oxygen production rate of this model under different IR separation wavelengths λ_3 (900 nm, 875 nm, 850 nm, 825 nm, 800 nm, 775 nm, and 750 nm) when the UV separation wavelength λ_2 = 385 nm and explores the optimal IR separation wavelength, as shown in Fig. 12.

Fig. 12a shows that with decreasing IR separation wavelength λ_3, the oxygen production rate $v_{O_2,pt}$ of the synergistic photothermal reaction slightly increases, and the oxygen production rate $v_{O_2,e}$ of electrolytic carbon dioxide decreases. Fig. 12b shows that with decreasing IR separation wavelength λ_3, the comprehensive oxygen production rate v_{O_2} continues to decrease. This shows that the effect of the reduction in the IR separation wavelength λ_3 on the reduction in the oxygen production rate $v_{O_2,e}$ of electrolytic carbon dioxide is greater than that on the increase in the oxygen production rate $v_{O_2,pt}$ of the synergistic photothermal reaction. Therefore, to ensure that the comprehensive model reaches the highest comprehensive oxygen production rate v_{O_2}, the IR separation wavelength λ_3 should be the highest value within the range as much as possible. The specific data are listed in Table 7.

4.4 Effect of the PV cell material on the oxygen production rate

This section explores the influence of different photovoltaic cell materials on the oxygen production rate while keeping the UV separation wavelength λ_2 = 385 nm and the electrolysis temperature T_e = 1235 K unchanged. PV cell materials affect mainly the IR separation wavelength λ_3 and photovoltaic conversion efficiency η_{PV} and then affect the oxygen production rate of the comprehensive model. This section explores the effects of five PV cell materials, including quadruple-junction GaAs, on the oxygen production rate to determine the material with the highest oxygen production rate. In this model, since the PV cell material only plays a small role in the heating process, the photovoltaic conversion efficiency changes with temperature are ignored and regarded as a certain value. The separation wavelengths and photovoltaic conversion efficiencies of the PV cell materials are shown in Table 8 (Ref. [16]).

Fig. 13 shows the oxygen production rates of different PV cell materials, from which we can see that the highest oxygen production rate can be achieved when CIGS is used, with a value of 3.5601×10^{-4} mol/s. This is mainly because the PETE device is the dominant part of the heating module, while the PV cells account for only a small part of the module, so its photovoltaic conversion efficiency has little effect on the oxygen production rate, and its separation wavelength plays a dominant role in the effect on the oxygen production rate. To achieve a relatively high oxygen production rate, PV cell materials with relatively large separation wavelengths, such as CIGS, can be selected.

5 Conclusions

In summary, a lunar oxygen production method combining a photothermal synergistic reaction and PV/PETE heating of electrolytic carbon dioxide is proposed. A model of the synergistic photothermal reaction, a model of PV/PETE heating and power generation, and a model for SOEC electrolysis of carbon dioxide were established. The oxygen production rates were investigated at different SOEC inlet temperatures T_e,

Table 6. Specific values of the synergistic photothermal reaction oxygen production rate, electrolytic carbon dioxide oxygen production rate, and comprehensive oxygen production rate under different UV separation wavelengths.

UV separation wavelength λ_2 (nm)	Photothermal synergistic reaction oxygen production rate $v_{O_2,pt}$ (mol/s)	Electrolytic oxygen production rate $v_{O_2,e}$ (mol/s)	Comprehensive oxygen production rate v_{O_2} (mol/s)
400	4.7318×10^{-5}	2.2722×10^{-4}	2.7454×10^{-4}
395	4.5554×10^{-5}	2.2961×10^{-4}	2.7517×10^{-4}
390	4.3675×10^{-5}	2.3173×10^{-4}	2.7541×10^{-4}
385	4.1677×10^{-5}	2.3377×10^{-4}	2.7545×10^{-4}
380	3.9652×10^{-5}	2.3569×10^{-4}	2.7534×10^{-4}
375	3.7096×10^{-5}	2.3799×10^{-4}	2.7509×10^{-4}
370	3.4655×10^{-5}	2.4014×10^{-4}	2.7480×10^{-4}
365	3.1963×10^{-5}	2.4247×10^{-4}	2.7443×10^{-4}
360	2.9665×10^{-5}	2.4442×10^{-4}	2.7408×10^{-4}

CSTR: 32290.14.JUSTC-2024-0062
DOI: 10.52396/JUSTC-2024-0062
JUSTC, **2025**, 55(2): 0201

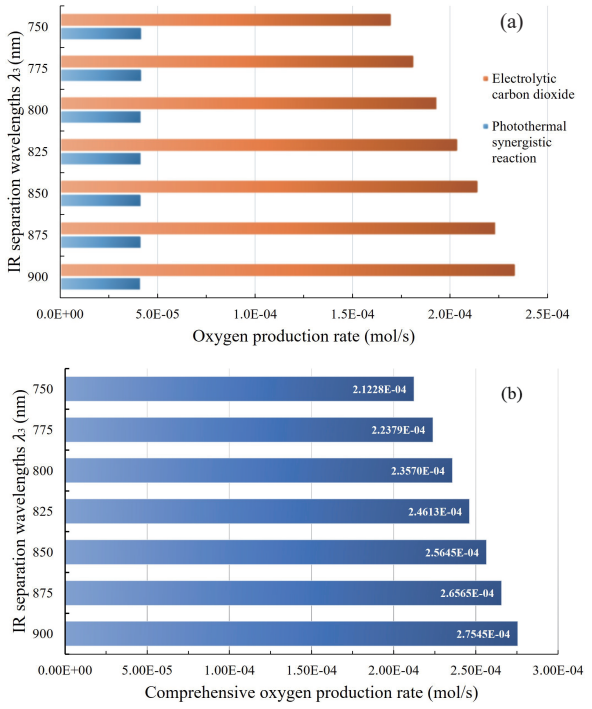

Fig. 12. (a) Oxygen production rate of the synergistic photothermal reaction with electrolytic carbon dioxide at different IR separation wavelengths. (b) Comprehensive oxygen production rate at different IR separation wavelengths.

UV separation wavelengths λ_2, IR separation wavelengths λ_3, and PV cell materials. The results indicated that (i) the inlet temperature of the SOEC should be increased as much as possible to convert more carbon dioxide into monoxide and oxygen to further increase the oxygen production rate; (ii) when the UV separation wavelength is approximately 385 nm, the proportion of solar energy allocated to the photoreaction and electrolysis cell is optimal, and the oxygen production rate is the highest, which is 2.7545×10^{-4} mol/s; (iii) within the allowable range, the IR separation wavelength should be increased as much as possible to increase the amount of solar radiation allocated to the electrolysis cell to improve the comprehensive oxygen production rate; and (iv) CIGS with a larger separation wavelength can be used as the PV cell material to obtain a higher oxygen production rate, which is 3.560×10^{-4} mol/s.

In this work, a PETE module is applied to solar full-spectrum oxygen generation for the first time, realizing the combination of high-temperature electrolysis of carbon dioxide and synergistic photothermal reactions. Compared with the single photothermal synergistic decomposition of water to produce oxygen and the single electrolysis of carbon dioxide to produce oxygen without spectral frequency division, this system produces oxygen at a higher rate of 2.7545×10^{-4} mol/s, compared with 5.3568×10^{-5} mol/s and 2.5244×10^{-4} mol/s under the same conditions, respectively. The use of solar energy and human respiratory emissions of carbon dioxide and water vapor to achieve in situ resource utilization on the Moon also suggests a feasible method for supplying the oxygen supply of the lunar human base.

Notably, owing to the long periodicity of solar radiation on

Table 7. Specific values of the synergistic photothermal reaction oxygen production rate, electrolytic carbon dioxide oxygen production rate and comprehensive oxygen production rate under different IR separation wavelengths.

IR separation wavelength λ_3 (nm)	Photothermal synergistic reaction oxygen production rate $v_{O_2,pt}$ (mol/s)	Electrolytic oxygen production rate $v_{O_2,e}$ (mol/s)	Comprehensive oxygen production rate v_{O_2} (mol/s)
900	4.1677×10^{-5}	2.3377×10^{-4}	2.7545×10^{-4}
875	4.1764×10^{-5}	2.2388×10^{-4}	2.6565×10^{-4}
850	4.1838×10^{-5}	2.1461×10^{-4}	2.5645×10^{-4}
825	4.1916×10^{-5}	2.0421×10^{-4}	2.4613×10^{-4}
800	4.1987×10^{-5}	1.9371×10^{-4}	2.3570×10^{-4}
775	4.2063×10^{-5}	1.8173×10^{-4}	2.2379×10^{-4}
750	4.2129×10^{-5}	1.7015×10^{-4}	2.1228×10^{-4}

Table 8. Separation wavelength and photovoltaic conversion efficiency of different PV cell materials.

PV cell materials	Separation wavelength λ_3 (nm)	Photovoltaic conversion efficiency η_{PV}
Quadruple-junction GaAs	900	37.2%
Triple-junction GaAs	900	29.8%
Si	1100	26.1%
CdTe	800	22.1%
CIGS	1200	23.4%

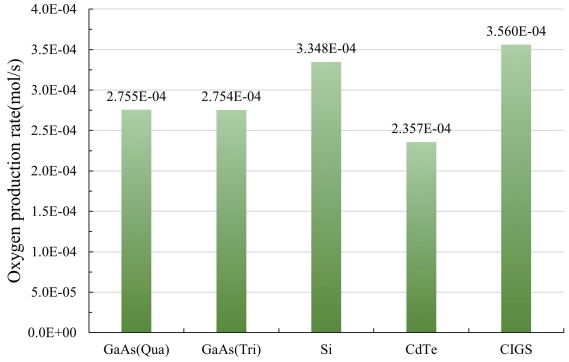

Fig. 13. Oxygen production rates of different PV cell materials.

CSTR: 32290.14.JUSTC-2024-0062
DOI: 10.52396/JUSTC-2024-0062
JUSTC, **2025**, 55(2): 0201

the Moon, an energy storage device may be required to store solar radiant energy in the form of electrical energy during long days so that the system can be operated properly during long nights. This aspect will be discussed in subsequent studies.

Data availability

The data that support the findings of this study are available upon reasonable request from the corresponding author.

Acknowledgements

The work was supported by the National Natural Science Foundation of China (52106276 and 52130601).

Conflict of interest

The authors declare that they have no conflict of interest.

Biographies

Wei Zhu is now pursuing his master's degree in Energy and Power at the University of Science and Technology of China. He graduated from Hefei University of Technology. His research mainly focuses on solar energy photothermal utilization.

Maobin Hu is an Associate Professor and Doctoral Supervisor at the School of Engineering Science, University of Science and Technology of China. His research mainly focuses on urban transportation, intelligent transportation, and energy conservation and emission reduction; solar energy, flow heat transfer, and thermal storage; network traffic, evolutionary game theory, and pedestrian flow.

References

[1] Hou J, Zhao C, Chang L, et al. General conception of future lunar exploration. *Manned Spaceflight*, **2015**, *21* (5): 425–434. (in Chinese)
[2] Sungchul H, Shin H S. Trend analysis of lunar exploration missions for lunar base construction. *Journal of Korea Academia-Industrial Cooperation Society*, **2018**, *19* (7): 144–152.
[3] Li M, Tong J Y, Wang Z H, et al. The research on lunar soil simulant production system. *Advanced Materials Research*, **2011**, *337*: 542–545.
[4] Yuan Y, Zhao C, Cao Y, et al. Research on distributed energy system of lunar surface research station. *Chinese Space Science and Technology*, **2023**, *43* (6): 32–42. (in Chinese)
[5] Hepp A F, Linne D L, Landis G A, et al. Production and use of metals and oxygen for lunar propulsion. *Journal of Propulsion and Power*, **1994**, *10*: 834–840.
[6] Protasova L, Snijkers F. Recent developments in oxygen carrier materials for hydrogen production via chemical looping processes. *Fuel*, **2016**, *181*: 75–93.
[7] Maes M, Gibilaro M, Chamelot P, et al. Lunar simulant behaviour in molten fluoride salt for ISRU applications. *Planetary and Space Science*, **2024**, *242*: 105854.
[8] Iisa K, Robichaud D J, Watson M J, et al. Improving biomass pyrolysis economics by integrating vapor and liquid phase upgrading. *Green Chemistry*, **2018**, *20*: 567–582.
[9] Wang M, Jiao H, Pu Z, et al. Ultra-high temperature molten oxide electrochemistry. *Angewandte Chemie International Edition*, **2022**, *61*: e202206482.
[10] Burke P A, Nord M E, Hibbitts C A, et al. Modeling electrolysis in reduced gravity: Producing oxygen from *in situ* resources at the Moon and beyond. *Frontiers in Space Technologies*, **2024**, *5*: 1304579.
[11] Zhong Y, Low J, Zhu Q, et al. *In situ* resource utilization of lunar soil for highly efficient extraterrestrial fuel and oxygen supply. *National Science Review*, **2023**, *10*: nwac200.
[12] Liu A, Shi Z, Hu X, et al. Lunar soil simulant electrolysis using inert anode for Al-Si alloy and oxygen production. *Journal of the Electrochemical Society*, **2017**, *164*: H126–H133.
[13] Li Z, Guo L, Peng K. Research on site selection of manned lunar base. *Manned Spaceflight*, **2015**, *21* (2): 158–162. (in Chinese)
[14] Miyahara H, Wen G, Cahalan R F, et al. Deriving historical total solar irradiance from lunar borehole temperatures. *Geophysical Research Letters*, **2008**, *35*: L02716.
[15] Li G, Li J, Dai Z, et al. Modelling and analysis of a novel hydrogen production approach by full spectrum solar energy. *Energy Conversion and Management*, **2022**, *263*: 115694.
[16] Tian J, Han R, Guo Q, et al. Direct conversion of CO_2 into hydrocarbon solar fuels by a synergistic photothermal catalysis. *Catalysts*, **2022**, *12*: 612.
[17] Witze A. NASA's Perseverance rover begins key search for life on Mars. *Nature*, **2022**, *606*: 441–442.
[18] McClean J B, Hoffman J A, Hecht M H, et al. Pre-landing plans for Mars Oxygen In-Situ Resource Utilization Experiment (MOXIE) science operations. *Acta Astronautica*, **2022**, *192*: 301–313.
[19] Hinterman E D, Khopkar P P. Reliability optimization of a Mars oxygen production plant. *Journal of Spacecraft and Rockets*, **2023**, *60*: 982–990.
[20] Hecht M, Hoffman J, Rapp D, et al. Mars Oxygen ISRU Experiment (MOXIE). *Space Science Reviews*, **2021**, *217*: 9.
[21] Rapp D, Inglezakis V J. Mars *in situ* resource utilization (ISRU) with focus on atmospheric processing for near-term application: A historical review and appraisal. *Applied Sciences*, **2024**, *14*: 653.
[22] Hoffman J A, Hecht M H, Rapp D, et al. Mars oxygen ISRU experiment (MOXIE)-preparing for human Mars exploration. *Science Advances*, **2022**, *8* (35): eabp8636.
[23] Wang H, Kong H, Pu Z, et al. Feasibility of high efficient solar hydrogen generation system integrating photovoltaic cell/photon-enhanced thermionic emission and high-temperature electrolysis cell. *Energy Conversion and Management*, **2020**, *210*: 112699.
[24] Li X Y, Wang S J, Cheng A Y. A lunar surface effective solar irradiance real-time model. *Chinese Journal of Geophysics*, **2008**, *51* (1): 25–30. (in Chinese)
[25] Xu C, Huang W, Li Z, et al. Photothermal coupling factor achieving CO_2 reduction based on palladium-nanoparticle-loaded TiO_2. *ACS Catalysis*, **2018**, *8*: 6582–6593.
[26] Yang F, Yang R, Yan L, et al. *In situ* growth of porous TiO_2 with controllable oxygen vacancies on an atomic scale for highly efficient photocatalytic water splitting. *Catalysis Science & Technology*, **2020**, *10*: 5659–5665.
[27] Montoya A T, Gillan E G. Enhanced photocatalytic hydrogen evolution from transition-metal surface-modified TiO_2. *ACS Omega*, **2018**, *3*: 2947–2955.
[28] Schneider J, Matsuoka M, Takeuchi M, et al. Understanding TiO_2 photocatalysis: Mechanisms and materials. *Chemical Reviews*, **2014**, *114*: 9919–9986.
[29] Li G, Li J, Yang R, et al. Performance analysis of a hybrid hydrogen production system in the integrations of PV/T power generation electrolytic water and photothermal cooperative reaction. *Applied Energy*, **2022**, *323*: 119625.
[30] Iora P, Aguiar P, Adjiman C S, et al. Comparison of two IT DIR-SOFC models: Impact of variable thermodynamic, physical, and flow properties. Steady-state and dynamic analysis. *Chemical Engineering Science*, **2005**, *60*: 2963–2975.
[31] Kribus A, Mittelman G. Potential of polygeneration with solar thermal and photovoltaic systems. *Journal of Solar Energy Engineering*, **2008**, *130*: 011001.

CSTR: 32290.14.JUSTC-2024-0062
DOI: 10.52396/JUSTC-2024-0062
JUSTC, **2025**, 55(2): 0201

[32] Wang H, Li W, Liu T, et al. Thermodynamic analysis and optimization of photovoltaic/thermal hybrid hydrogen generation system based on complementary combination of photovoltaic cells and proton exchange membrane electrolyzer. *Energy Conversion and Management*, **2019**, *183*: 97–108.
[33] Schwede J W, Bargatin I, Riley D C, et al. Photon-enhanced thermionic emission for solar concentrator systems. *Nature Materials*, **2010**, *9*: 762–767.
[34] Sharma S, Stanley R, Kumari N. Electrochemical modeling and simulation of CO_2 reduction in solid oxide electrolysis cells. *Journal of Hazardous, Toxic, and Radioactive Waste*, **2022**, *26*: 04022005.
[35] Ni M. Modeling of a solid oxide electrolysis cell for carbon dioxide electrolysis. *Chemical Engineering Journal*, **2010**, *164*: 246–254.
[36] Ni M, Leung M K H, Leung D Y C. Parametric study of solid oxide steam electrolyzer for hydrogen production. *International Journal of Hydrogen Energy*, **2007**, *32*: 2305–2313.
[37] Ni M, Leung M K H, Leung D Y C. A modeling study on concentration overpotentials of a reversible solid oxide fuel cell. *Journal of Power Sources*, **2006**, *163*: 460–466.
[38] Hernández-Pacheco E, Singh D, Hutton P N, et al. A macro-level model for determining the performance characteristics of solid oxide fuel cells. *Journal of Power Sources*, **2004**, *138*: 174–186.
[39] Zhang H, Wang J, Su S, et al. Electrochemical performance characteristics and optimum design strategies of a solid oxide electrolysis cell system for carbon dioxide reduction. *International Journal of Hydrogen Energy*, **2013**, *38*: 9609–9618.
[40] Ibrahim N S, Leaw W L, Mohamad D, et al. A critical review of metal-doped TiO_2 and its structure–physical properties–photocatalytic activity relationship in hydrogen production. *International Journal of Hydrogen Energy*, **2020**, *45*: 28553–28565.
[41] Ebbesen S D, Mogensen M. Electrolysis of carbon dioxide in solid oxide electrolysis cells. *Journal of Power Sources*, **2009**, *193*: 349–358.

CSTR: 32290.14.JUSTC-2024-0062
DOI: 10.52396/JUSTC-2024-0062
JUSTC, **2025**, 55(2): 0201